aerospace

MDPI

Article

Study of Ultra-High-Speed Rarefied Flow for Nozzle Optimization with Multiscale Particle Simulations

Wenjin Sun [1,2], Yuan Hu [1,2,*], Fei Fei [3], Chao Yang [4], Jinwen Cao [1], Xian Meng [1], Quanhua Sun [1,2] and Heji Huang [1,2,*]

[1] State Key Laboratory of High Temperature Gas Dynamics, Institute of Mechanics, Chinese Academy of Sciences, Beijing 100190, China
[2] School of Engineering Science, University of Chinese Academy of Sciences, Beijing 100049, China
[3] School of Aerospace Engineering, Huazhong University of Science and Technology, Wuhan 430074, China
[4] Wide Range Flight Engineering Science and Applications Center, Institute of Mechanics, Chinese Academy of Sciences, Beijing 100190, China
* Correspondence: yhu@imech.ac.cn (Y.H.); huang@imech.ac.cn (H.H.)

Abstract

Ultra-high-speed rarefied gas wind tunnels (RGWTs) are critical for estimating the aerodynamic forces acting on spacecraft in very low Earth orbit (VLEO). These tunnels utilize nozzles with large expansion ratios to generate extreme freestream conditions ($Ma > 20$, $Kn > 1$). However, the large expansion ratio induces a multiscale flow within the nozzle that simultaneously spans the continuum and transitional regimes, making the investigation of such flows extremely challenging. The present work applies a multiscale particle method to investigate the RGWT nozzle flow in a unified manner. Simulations reveal that the nozzle flow is underexpanded and characterized by rarefaction effects, and can be categorized into a central core and a surrounding region comprising the shock wave and boundary layer. This surrounding region occupies a significant portion of the nozzle exit, notably degrading flow quality. The wall suction technique increases the uniform flow radius by 11% at a total pressure of 500 kPa, while its effectiveness is limited at 50 kPa due to heightened rarefaction. Finally, a wall smoothing technique is proposed to improve the quality of nozzle flow by recognizing that strongly rarefied flows are governed by gas-surface interactions.

Keywords: very low Earth orbit (VLEO); rarefied gas wind tunnel (RGWT); ultra-high-speed multiscale flow; rarefaction effect; flow-field optimization; underexpanded flow

Academic Editor: Kung-Ming Chung

Received: 31 March 2026
Revised: 11 June 2026
Accepted: 12 June 2026
Published: 16 June 2026

1. Introduction

The very low Earth orbit (VLEO), a new space frontier generally acknowledged to be in the range of 100–350 km, opens up many new missions, such as ultra-high-resolution ground observation and imaging [1], high-precision Earth's gravity mapping [2], low-latency communications [3], etc. These new possibilities are driving both government and commercial efforts to exploit the VLEO. However, the drastically increased atmospheric drag makes long-duration operation of VLEO satellites and, thereby, the exploitation of the VLEO very challenging. To mitigate the appreciable drag, various advanced propulsion strategies are under active development. Air-breathing electric propulsion (ABEP) is such a representative solution [4,5]. It collects and stores the environmental gases as propellant for electric propulsion systems to enable longer missions at VLEO altitudes. However, ABEP suffers from several challenges, including the efficient collection and compression of

rarefied atmospheric gases, and the stable discharge of air propellants [5], so technologies aside from drag compensation are desired to meet the requirements for sustaining satellites in the VLEO. For example, several groups have recently proposed drag-reduction strategies for VLEO satellite design [6–8], which offer promising measures to alleviate the burden on propulsion systems for a VLEO satellite. Accurate prediction of aerodynamic forces is essential for these design and optimization tasks, as well as for scientific missions requiring precise attitude control and ultra-fine drag compensation [9,10].

The atmospheric density at the VLEO is so low that the flow around a vehicle belongs to the rarefied regime, namely from the transitional to free-molecular flow regime [7,8,11]. Moreover, the flow speed is extremely high, exceeding 5 km/s. For high-speed rarefied flows, the numerical computation, particularly the Direct Simulation Monte Carlo (DSMC) method [12], serves as the primary tool to estimate aerodynamic performance. DSMC is sufficiently sophisticated to provide valuable information on rarefied aerodynamics, whereas it depends on the reliability of the models for gas-surface interaction (GSI). Unfortunately, considerable uncertainties remain when applying the available GSI models under highly rarefied conditions with ultra-high impact speeds [12]. Therefore, ground-based experiments are necessary to enhance the confidence in predicting aerodynamic forces for VLEO satellites.

A few rarefied gas wind tunnels (RGWTs) [13,14] have been developed worldwide based on the Mach–Knudsen ($Ma - Kn$) scaling law. These facilities can achieve maximum Ma of 10 and Kn of 1 (with Kn evaluated using a characteristic length of 5 mm) approximately. However, a freestream of $Ma > 20$ and $Kn > 1$ is required to reproduce the operating environment for VLEO satellites. Moreover, the available test section of the existing RGWTs is very small, limiting the size of test models. For example, the radius of the cross-section with uniform freestream is about 10 mm in the JAXA facility [13]. In addition to the $Ma - Kn$ similarities, the geometrical similarity must also be satisfied in wind tunnel experiments. The limited size of the uniform freestream region poses a challenge to the ground testing of VLEO satellites, as these vehicles often possess fine aerodynamic configurations (e.g., the wings and tail fins) [7,9], for which substantial downscaling is difficult while maintaining geometric fidelity.

A large-sized ultra-high-speed RGWT, named XBF, is under development primarily for VLEO applications at the Institute of Mechanics, Chinese Academy of Sciences (CAS). XBF utilizes a plasma heating generator and a nozzle with extremely large expansion ratio to generate high-speed rarefied freestream, an approach previously demonstrated in a small-sized wind tunnel [15,16]. To facilitate the evaluation of aerodynamic performance of VLEO satellites, XBF should be capable of generating flow conditions of $Ma > 20$ and $Kn > 1$ with Kn evaluated using a characteristic length no smaller than 100 mm. This requirement implies that the cross-sectional radius of the uniform freestream region must be an order of magnitude larger than those of previous facilities. To achieve this goal, it is essential to understand the physics of nozzle-expansion flows, which dictates the freestream property, and to develop possible nozzle optimization strategies for improving flow quality.

Due to the extremely large expansion ratio, the nozzle flow is inherently multiscale and may simultaneously experience all flow regimes, namely the continuum, slip, transitional, and free molecular regimes. This multiscale nature makes accurate prediction of nozzle flows extremely challenging. Early studies [17–20] often employed the CFD-DSMC hybrid approach to address such multiscale flows. However, selecting an appropriate coupling strategy for the two fundamentally different solvers remains challenging [21]. As an alternative, unified solvers such as the unified gas-kinetic scheme (UGKS) [22], the discrete unified gas-kinetic scheme (DUGKS) [23], and other deterministic kinetic solvers [24,25]

based on the Shakhov [26] or Holway [27] models have been developed to capture multiscale nonequilibrium flows. However, for high-speed flows, these deterministic methods generally require fine discretization of the velocity space, resulting in substantial memory consumption and computational cost. Meanwhile, particle-based kinetic methods, such as the particle Bhatnagar–Gross–Krook (BGK) [28,29] and particle Fokker–Planck (FP) methods [30], have also been developed for multiscale flows. Recently, the Unified Stochastic Particle BGK (USPBGK) method was proposed by Fei et al. [31]. By incorporating collision effects into the transport process, USPBGK improves the computational efficiency for multiscale flows.

Earlier experimental studies have shown that wall suction is an effective technique for improving the freestream quality of the nozzle flows in the nozzle for low-density wind tunnels [32–35]. This technique typically employs a vacuum pumping system connected to porous nozzle walls to remove low-momentum gas near the wall, thus reducing the thickness of the boundary layer. However, these studies have mainly focused on nozzles generating freestream conditions of $Ma < 10$ and $Kn < 0.1$. The effectiveness of wall suction under more rarefied flow conditions remains uncertain and warrants further investigation.

There are few reported RGWTs capable of providing freestream conditions required by VLEO ground testing ($Ma > 20$, $Kn > 1$). To generate such freestreams, RGWT nozzles require much larger expansion ratios than those used in previous facilities, resulting in substantially more complex nozzle flows with strong multiscale features than before. However, the understanding of multiscale flows inherent in the RGWT nozzles is poor. Likewise, the applicability of previous flow quality improvement means, such as the wall suction, to the VLEO testing facilities is unexplored. In this work, a multiscale particle method (USPBGK-DSMC) is employed to numerically simulate the flow in an RGWT nozzle with an extremely large expansion ratio. A continuum-based simulation is also carried out, and the continuum results are directly compared with the particle solutions to reveal the multiscale characteristics of the flows. The effect of wall suction on flow quality, particularly the uniformity of density and velocity, is further investigated under different rarefaction conditions. Considering the reduced effectiveness of wall suction in strongly rarefied flows, a wall smoothing optimization strategy is proposed. The remainder of this paper is organized as follows: Section 2 introduces the numerical methods used in the study. Section 3 describes the nozzle geometry and simulation conditions. Section 4 presents and discusses the results. Finally, the key findings of this work are summarized in Section 5.

2. Numerical Methods

2.1. Multiscale Particle Method

The DSMC method is the most successful kinetic method for simulating nonequilibrium gas flows [12]. However, its computational cost becomes prohibitive in near-continuum regimes because the cell size and time step must remain smaller than the local mean free path and mean collision time [36,37]. To improve computational efficiency in near-continuum flows, particle kinetic methods, such as particle BGK [28,29] and particle Fokker–Planck methods [30], have been developed. However, the conventional BGK model yields an incorrect Prandtl number ($Pr = 1$). To address this issue, advanced kinetic models [26,27], such as the Ellipsoidal Statistical BGK (ESBGK) model [27], have been proposed. However, when the time step exceeds the mean collision time, the transport coefficients will deviate significantly from physical values. This limitation restricts the application of the particle ESBGK method to near-continuum flows.

To overcome this limitation, Fei et al. [31] proposed the USPBGK method, which incorporates collision effects into the transport process, thereby relaxing the restrictions on time step. The governing equations of the USPBGK method are given by:

$$\frac{\partial f}{\partial t} + c_i \frac{\partial f}{\partial x_i} - J_{USPBGK} = \frac{1}{\tau_{BGK}}(f_G - f) - J_{USPBGK} \quad (1)$$

$$J_{USPBGK} = \frac{P_c}{\tau_{BGK}}(f_M - f_{Grad}) \quad (2)$$

where f denotes the particle distribution function, c_i is the particle velocity, and τ_{BGK} is the relaxation time. f_G represents the anisotropic Gaussian distribution function, P_c is a scaling parameter, f_M is the Maxwellian distribution function, and f_{Grad} is the Grad's 13-moment distribution function.

For highly rarefied flows, Fei and Jenny [38] further coupled USPBGK with DSMC to improve the accuracy in nonequilibrium regions. The governing equation is

$$\frac{\partial f}{\partial t} + c_i \frac{\partial f}{\partial x_i} - (1 - P_s) J_{USPBGK} = P_s J_{Boltzmann} + (1 - P_s)\left[\frac{1}{\tau_{BGK}}(f_G - f) - J_{USPBGK}\right] \quad (3)$$

where $J_{Boltzmann}$ represents the collision term in the Boltzmann equation, and P_s is a switching parameter used to divide the computational domain into USPBGK and DSMC regions. When $P_s = 0$, Equation (3) reduces to Equation (1), and the USPBGK method is employed. Conversely, when $P_s = 1$, Equation (3) reduces to the Boltzmann equation, and the DSMC method is employed. Recently, the USPBGK-DSMC method has been further developed for the simulation of polyatomic gas flows [39,40].

The USPBGK-DSMC method employs simulation particles to represent a much larger number of real molecules. For multiscale flows with large density variations, the use of a fixed particle weight may result in excessive particles in continuum regions and insufficient particles in rarefied regions. To improve the computational efficiency while maintaining accuracy, the variable particle-weight technique proposed by Boyd [41] is employed in the present study.

GSI plays an important role in nozzle flows. Recent research [42] has demonstrated that DSMC simulations of flow in the Rothe nozzle [43] show excellent agreement with experimental density and temperature profiles when a diffusely reflecting wall with full thermal accommodation is employed. Accordingly, a diffusely reflecting wall with full thermal accommodation is assumed for the interactions between gas and nozzle walls in this work.

2.2. Continuum Method

To reveal the multiscale characteristics of the flow in the nozzle, a continuum approach based on the Navier–Stokes (NS) equations is also employed. The NS equations, encompassing continuity, momentum, and energy equations, are discretized through the finite-volume scheme. The inlet boundary conditions are defined by the total pressure and total temperature. Extrapolation boundary conditions are applied at the outlet because the flow is supersonic. Considering the rarefaction effect present in the nozzle flow, first-order slip conditions are imposed at the wall. The first-order velocity slip and temperature jump boundary conditions are expressed as

$$u_g - u_w = \frac{2-\sigma_u}{\sigma_u}\lambda\left(\frac{\partial u}{\partial n}\right)_w \tag{4}$$

$$T_g - T_w = \frac{2-\sigma_T}{\sigma_T}2\lambda\left(\frac{\partial T}{\partial n}\right)_w \tag{5}$$

where u is the velocity, T represents the temperature, subscripts w and g denote the wall and the gas adjacent to the wall, n indicates the wall-normal direction, σ_u is the tangential momentum accommodation coefficient, and σ_T is the thermal accommodation coefficient. Both σ_u and σ_T are assumed to be 1, consistent with the GSI model employed in the particle simulations.

2.3. Validation Study

As the nozzle flow spans multiple flow regimes, it is necessary to verify the accuracy of the multiscale particle method. In our previous work [44], the flow in a planar wedge-shaped nozzle originally studied by Fei and Jenny [38] was simulated using the present numerical method. The predicted results obtained using both the multiscale particle and continuum methods showed good agreement with the reference data, demonstrating the capability of the present methods for multiscale nozzle-flow simulations.

To further validate the accuracy of the present particle method, an additional benchmark simulation of hypersonic flow past a circular cylinder is conducted. The same computational conditions as those reported by [45] are adopted. Argon is used as the working gas, with a freestream velocity of 2634.1 m/s (Mach 10) and a freestream temperature of 200 K. The cylinder diameter is 0.3048 m, and the wall temperature is fixed at 500 K. The computational domain and grid are shown in Figure 1. Based on the freestream conditions and cylinder diameter, the corresponding Knudsen number is approximately 0.002.

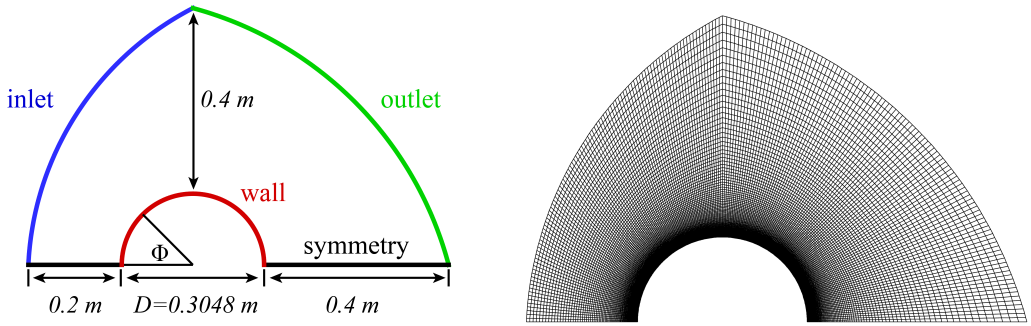

(**a**) (**b**)

Figure 1. (**a**) Computational domain and (**b**) corresponding grid for the cylinder case.

Figure 2 compares the predicted temperature distribution along the stagnation streamline and the velocity distribution along the line normal to the cylinder surface at an angle of 90°. The present particle-method results show good agreement with the DSMC data reported in [45], indicating the reliability and accuracy of the present particle simulation method.

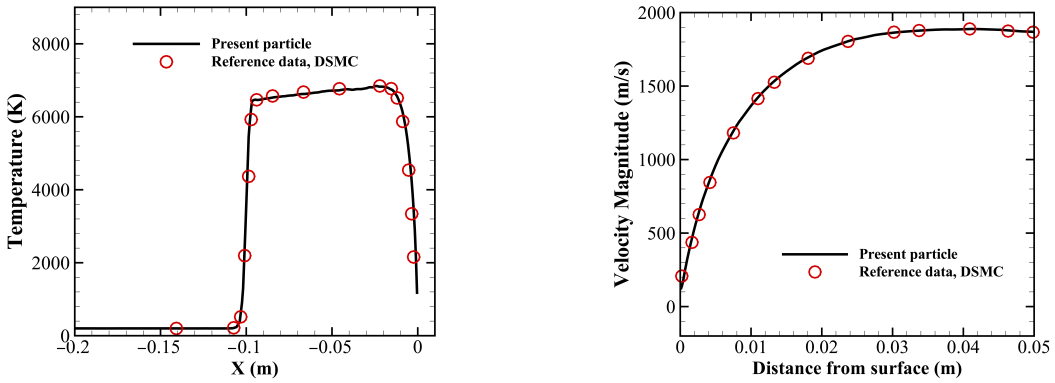

Figure 2. (**a**) Static temperature along the stagnation line and (**b**) velocity magnitude along a line normal to the body surface at $\Phi = 90°$. The reference data are from the DSMC results in [45].

3. Physical Models and Numerical Settings

3.1. Nozzle Configuration

The present study adopts a nozzle configuration based on the hypersonic nozzle employed in the MARHy RGWT [14]. The nozzle in MARHy facility has a conical contour with a half-opening angle of 15°. Considering the significant rarefaction effects encountered in VLEO conditions, a larger half-opening angle of about 30° is adopted in the present design to mitigate boundary-layer growth within the nozzle. The divergent section is contoured using a convex arc wall to minimize the exit-flow angle.

The nozzle is axisymmetric and consists of a convergent section with a length of 0.01 m, a straight section with a length of 0.002 m, and a divergent section with a length of 0.3 m. To achieve ultra-high-speed flow conditions, the nozzle employs a narrow throat with a radius of $R_t = 0.002$ m and a large exit with a radius of $R_e = 0.155$ m, yielding an expansion ratio of 6006. According to quasi-one-dimensional flow theory [46], the pressure decreases by approximately seven orders of magnitude throughout the nozzle because of the extremely large expansion ratio, thereby enabling the generation of a rarefied freestream at the nozzle exit.

The computational domain is also shown in Figure 3a. The exit domain is extended to ensure the accuracy of the simulations [47]. Different colors are used to indicate the boundary types in the computational domain. As shown in Figure 3a, the blue lines denote the inlet boundary, the red lines represent the wall boundary, the green lines indicate the outlet boundary, and the black lines correspond to the nozzle axis. To investigate the effect of the wall suction on the flow, six suction pores are distributed along the wall of the divergent section. As illustrated in Figure 3b, the centers of the pores are located between $Z = 0.01$ m and $Z = 0.25$ m with an interval of 0.05 m. The width of each pore is set to 0.25 times the local nozzle radius at the pore center location. In the simulations, these pores are treated as outlet boundaries (green lines).

3.2. Computational Settings

In this study, atomic oxygen is selected as the propellant gas for two primary reasons: (1) atomic oxygen constitutes a major component of the VLEO atmosphere, and its volume fraction increases significantly with increasing orbital altitude; (2) the high-enthalpy gas generated by the plasma generator reaches extremely high temperatures (on the order of 10,000 K), resulting in the complete dissociation of oxygen molecules upstream of the nozzle. To assess the importance of recombination in the nozzle expansion section, the Damköhler number (Da) is estimated using the nozzle-exit flow conditions predicted

by quasi-one-dimensional theory [46]. Considering the recombination reaction of atomic oxygen, the estimated Da is approximately 10^{-9}, indicating that the chemical reaction timescale is much larger than the flow timescale. Therefore, the nozzle expansion flow can reasonably be treated as chemically frozen, and a frozen composition resulting from upstream chemical reactions is considered in this study.

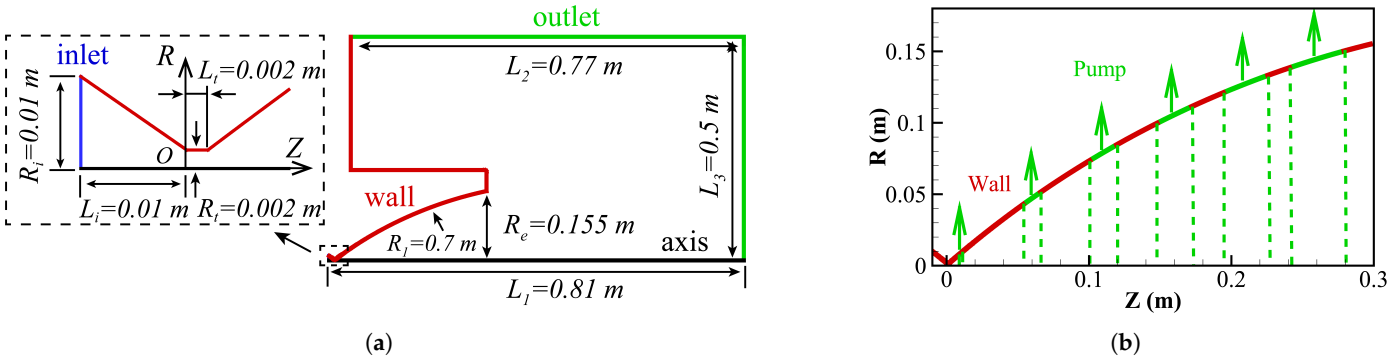

Figure 3. (**a**) Computational domain and (**b**) distribution of the suction pores in the divergent section.

At the inlet, the total temperature T_0 is fixed at 10,000 K, and the total pressure P_0 is set to 500 kPa and 50 kPa for different cases. The inlet total pressures are selected based on Knudsen number similarity considerations for RGWT applications. The case with P_0 = 500 kPa corresponds to near-free-molecular flow conditions ($Kn \approx 10$) in the nozzle plume, based on a representative model with a characteristic length of 0.01 m, which is comparable to the model scales commonly adopted in the JAXA HRWT facility [13]. The inclusion of the 50 kPa case allows for the investigation of flow characteristics under even stronger rarefaction conditions. The nozzle wall temperature is maintained at T_w = 373 K. All outlet boundaries are treated as vacuum boundaries because the pumping system maintains the ambient pressure at a level much lower than the flow pressure.

To provide an overall characterization of the degree of rarefaction effect, the Knudsen number is defined as

$$Kn = \frac{\lambda}{D} \tag{6}$$

where λ is the local mean free path and D is the characteristic length. In the present study, the nozzle throat diameter and nozzle exit diameter are adopted as the characteristic lengths for defining the throat Knudsen number (Kn_t) and exit Knudsen number (Kn_e), respectively. The mean free path is evaluated using the Variable Hard Sphere (VHS) model as

$$\lambda = \frac{1}{\sqrt{2}\pi d_{ref}^2 n \left(T_{ref}/T\right)^{\omega-1/2}} \tag{7}$$

where d_{ref}, T_{ref}, and ω denote the reference molecular diameter, reference temperature, and viscosity exponent in the VHS model, respectively. Here, n is the number density and T is the static temperature.

The computational conditions and corresponding Knudsen numbers for the simulated cases are summarized in Table 1. The values of Kn_t and Kn_e are obtained by area-averaging the local Knudsen numbers over the nozzle throat and exit cross sections, respectively. As shown in Table 1, the flow evolves from continuum conditions near the nozzle throat to rarefied conditions near the nozzle exit, demonstrating the multiscale nature of the present nozzle flow and the necessity of employing multiscale simulation methods.

Table 1. Computational conditions and corresponding Knudsen numbers for the simulated cases.

Case	P_0, kPa	T_0, K	Kn_t	Kn_e
1	500	10,000	1.4×10^{-4}	0.014
2	50	10,000	1.2×10^{-3}	0.15

To ensure numerical accuracy, grid-independence and particle-convergence studies are conducted for the case of $P_0 = 500$ kPa. As shown in Figure 4a, the number of grid cells in the radial direction at the nozzle throat is denoted as $N_{cell,r}$, while the number of particles per cell is denoted as N_p. Three grid resolutions, i.e., $N_{cell,r} = 40$, 80, and 160, together with three particle numbers, i.e., $N_p = 100$, 200, and 300, are examined.

Figure 4b shows the static pressure distributions along the nozzle centerline for different grid resolutions and particle numbers. The predicted pressure distribution exhibits negligible variation with further grid refinement for $N_{cell,r} \geq 80$. In addition, the solutions obtained with $N_p = 200$ and 300 are nearly identical, indicating that particle convergence has been obtained. Considering the balance between computational cost and accuracy, the grid with $N_{cell,r} = 80$ and $N_p = 200$ is adopted for all simulations presented in the remainder of this paper.

The computational time step used in the present simulations is $\Delta t = 5 \times 10^{-8}$ s. The time step is selected to satisfy $CFL_{max} < 1$ for USPBGK calculations and to remain smaller than the local mean collision time for DSMC calculations. In the particle simulations, the VHS model is employed for the DSMC method. The reference molecular diameter for atomic oxygen is $d_{ref} = 3.29 \times 10^{-10}$ m, and the viscosity exponent is $\omega = 0.736$ [48].

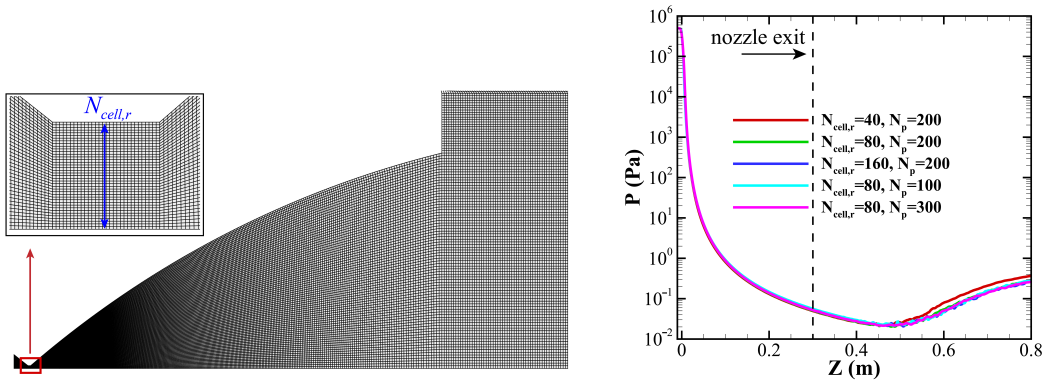

(**a**) (**b**)

Figure 4. (**a**) Computational grid and (**b**) static pressure distribution along the nozzle axis for different grid resolutions and particle numbers.

4. Results and Discussions

In this section, we first present the results for a total pressure of P_0 = 500 kPa. The multiscale characteristics of the underexpanded flow in the nozzle are discussed. The effects of the wall suction on the nozzle flow are also analyzed. Subsequently, we focus on the results obtained at a lower total pressure of P_0 = 50 kPa. A comparison of the nozzle flow between P_0 = 500 kPa and P_0 = 50 kPa is presented. The effects of wall suction are further examined, and a novel technique aimed at improving the flow uniformity is finally proposed.

4.1. Nozzle Flow for P_0 = 500 kPa

4.1.1. Multiscale Characteristics

Figure 5 shows the comparisons of the static pressure contours and static pressure profiles along the nozzle centerline obtained by the particle and continuum methods, respectively. It is seen that the pressure decreases monotonically by nearly seven orders of magnitude from the nozzle inlet to the nozzle exit. This large pressure variation differs from that reported in previous studies of nozzle flows in the low-density wind tunnels, where the pressure decrease is typically less than five orders of magnitude [43,49]. As a result of this substantial pressure variation, the flow exhibits multiscale characteristics. Specifically, the flow may simultaneously experience several flow regimes, including the continuum, slip, transitional, and even free molecular flow regimes, under which the continuum method may break down. The pressure distributions depicted in Figure 5 clearly reveal the multiscale nature of the nozzle flow. The particle and continuum methods obtain nearly identical results in the region where $Z \leq 0.2$ m, indicating that the flow remains within the continuum regime. Conversely, in the region where $Z > 0.2$ m, the continuum results show evident discrepancies compared with the particle results, suggesting the breakdown of the continuum assumption.

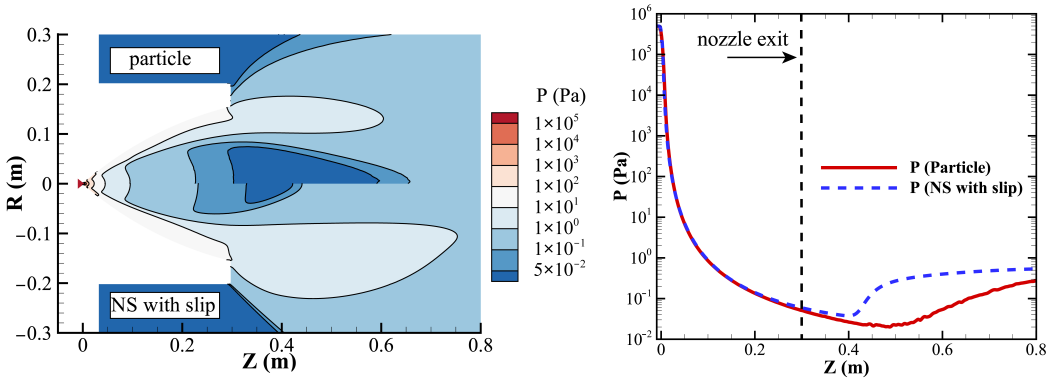

Figure 5. (**a**) Static pressure contours and (**b**) centerline static pressure distributions predicted by different methods.

To quantitatively assess the validity of the continuum assumption, continuum breakdown parameters are commonly employed. Among various continuum breakdown parameters [50–53], the gradient-length local Knudsen number Kn_{GLL} proposed by Boyd [52] has demonstrated strong predictive capability. Kn_{GLL} is defined as follows:

$$Kn_V = \frac{\lambda}{V}|\nabla V| \tag{8}$$

$$Kn_T = \frac{\lambda}{T}|\nabla T| \tag{9}$$

$$Kn_\rho = \frac{\lambda}{\rho}|\nabla \rho| \tag{10}$$

$$Kn_{GLL} = \max(Kn_V, Kn_T, Kn_\rho) \tag{11}$$

where V, T, and ρ represent the velocity magnitude, static temperature, and density, respectively.

Figure 6a illustrates the distribution of Kn_{GLL} contours within the nozzle. As Kn_{GLL} spans approximately three orders of magnitude from the nozzle inlet to the nozzle exit, the flow exhibits the multiscale characteristics clearly. Previous studies have shown that continuum method predictions deviate significantly from DSMC results in regions where

$Kn_{GLL} > 0.05$ [52]. Since Kn_{GLL} exceeds 0.05 over most of the divergent section, large discrepancies between continuum and particle-based solutions are expected in this region. The relative error between the continuum and particle-based results is shown in Figure 6b, where the error is defined as the maximum normalized discrepancy in velocity, temperature, and density, i.e.,

$$Error_{max} = \max(Error_V, Error_T, Error_\rho) \tag{12}$$

The contour line of $Kn_{GLL} = 0.15$ is also superimposed on Figure 6b. The result indicates that the continuum-solution error closely follows the distribution of Kn_{GLL}. The discrepancy between the continuum and particle solutions increases rapidly with the increase in Kn_{GLL} and reaches approximately 25% at $Kn_{GLL} = 0.15$, indicating the breakdown of the continuum assumption. The pronounced variation in Kn_{GLL} and the extensive continuum breakdown region indicate the necessity of employing a multiscale particle-based approach for accurate and efficient prediction of the nozzle flow.

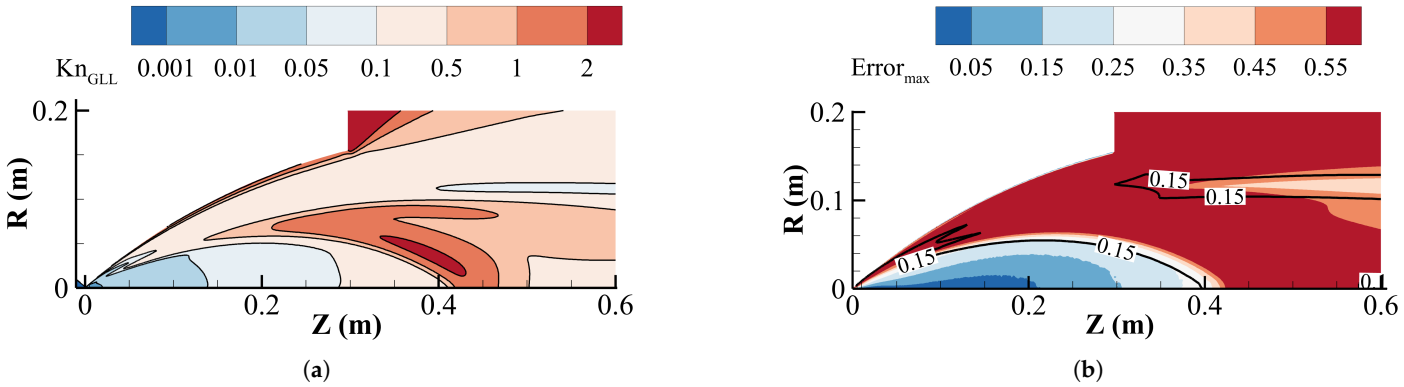

Figure 6. (**a**) Kn_{GLL} contours and (**b**) relative error contours between the particle and continuum results.

Given the limitations of continuum methods under these conditions, the subsequent analysis in this paper is based on results obtained from particle simulations.

In addition to continuum breakdown, the importance of chemical reactions in the nozzle flow is also evaluated using the Damköhler number, which is defined as the ratio of the characteristic flow timescale τ_f to the characteristic chemical reaction timescale τ_c :

$$Da = \frac{\tau_f}{\tau_c} = \frac{L/V_z}{\rho/\dot{\omega}} \tag{13}$$

where τ_f is estimated from the ratio of the nozzle expansion-section length ($L = 0.3$ m) to the axial velocity V_z, while τ_c is estimated from the ratio of the local density ρ to the net chemical production rate $\dot{\omega}$.

Figure 7a shows the Damköhler number contours in the nozzle flow. The results indicate that the Damköhler number in the nozzle expansion section is much smaller than unity ($Da \ll 1$), suggesting that the flow in the expansion region can reasonably be treated as chemically frozen. Figure 7b further presents the distributions of the Damköhler number and static temperature along the nozzle axis. Although the Damköhler number approaches unity near the throat and upstream regions, where the temperature exceeds 4000 K, these regions mainly correspond to the high-temperature dissociated state of oxygen. Since the present work mainly focuses on the rarefied flow in the nozzle expansion section, the chemically frozen assumption is considered reasonable.

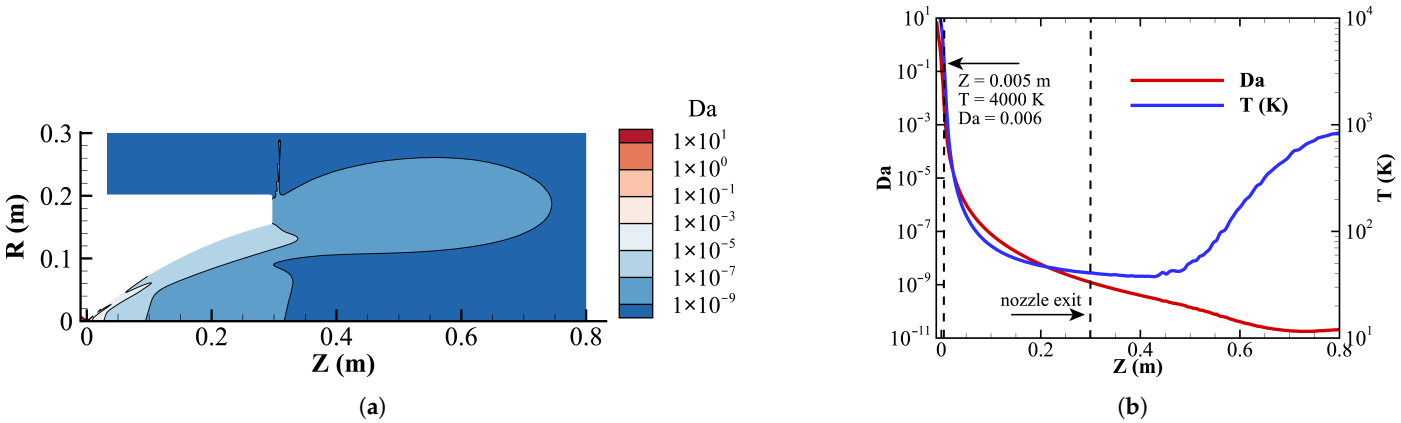

Figure 7. (**a**) Damköhler number contours and (**b**) distributions of the Damköhler number and static temperature along the nozzle axis.

4.1.2. Underexpanded Flow

It is interesting to note from Figure 5b that the pressure predicted by the particle method initially decreases but then increases downstream of the nozzle exit. This behavior strongly suggests that the gas is compressed by a shock wave, resulting in an increase in density. Figure 8a presents the density and Mach number contours in the nozzle flow. As expected, an increase in density and a decrease in Mach number are observed outside the nozzle exit. The streamlines in Figure 8a undergo noticeable deflection near the nozzle outlet, providing additional evidence for the presence of a shock wave. One can further examine the distribution of flow variables along the streamlines. As shown in Figure 8b, both the density and static temperature increase markedly along the two streamlines, confirming the existence of the shock wave. Figure 8b also shows that the increase in temperature precedes the increase in density. This behavior can be attributed to the bimodal velocity distribution in the shock structure, where the molecular samples consist primarily of undisturbed molecules, with only a small fraction affected by the shock wave [54].

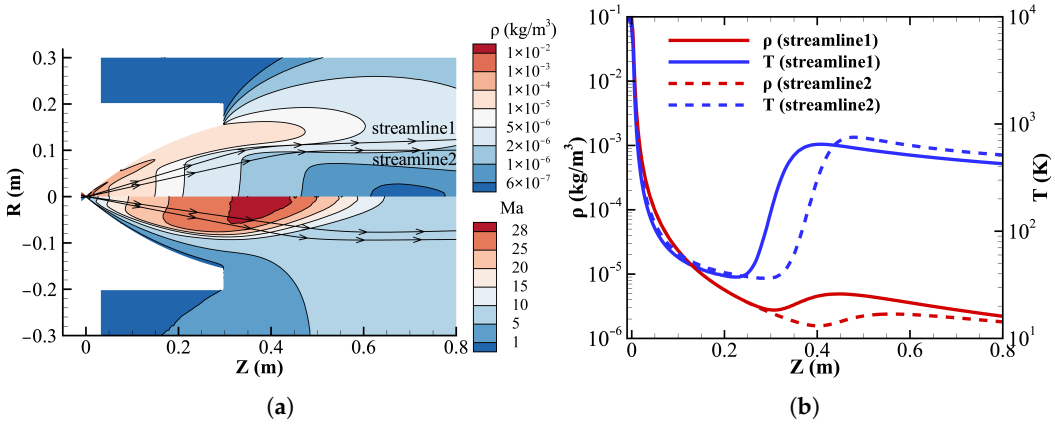

Figure 8. (**a**) Density and Mach number contours and (**b**) density and static temperature distributions along the streamlines.

Figure 9 presents the density distribution at the nozzle exit. The density exhibits a bimodal distribution, which is a characteristic feature of the underexpanded flow [43,55–58]. As a result, the flow in the nozzle can be divided into two distinct regions: a central core flow region and a surrounding region composed of shock wave and boundary layer. Figure 9 shows that the core flow region exhibits excellent uniformity and can therefore be regarded as the effective test region for wind tunnel experiments [13,14]. As shown in Figure 9, the

region of the shock wave and boundary layer accounts for approximately 50% of the nozzle exit area under the present low-density conditions. This limits the application of the nozzle by reducing the available flow area and leading to a decrease in the expansion ratio. To overcome this issue, optimization of the nozzle flow is required.

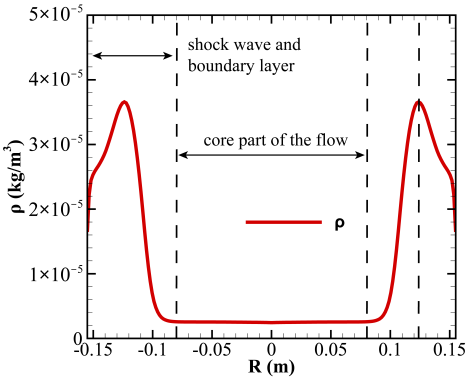

Figure 9. Density distribution at the nozzle exit.

4.1.3. Effect of Wall Suction

Wall suction has been widely used as an effective technique for nozzle optimization in traditional low-density wind tunnels. Figure 10 presents the density contours and the density distributions at the nozzle exit for both the suction-wall nozzle and the solid-wall nozzle. Compared with the solid-wall nozzle, wall suction reduces the density in the region of shock wave and boundary layer, thereby increasing the area of the core flow region. This observation is consistent with the previous experimental studies of the low-density nozzles [32,33].

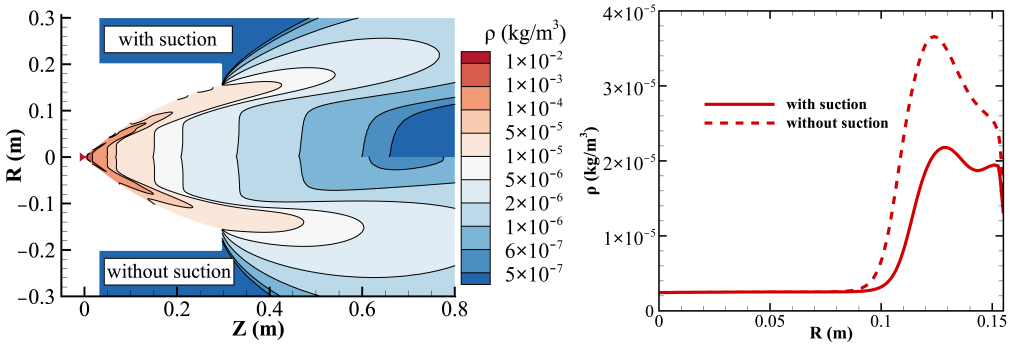

(**a**) (**b**)

Figure 10. (**a**) Density contours and (**b**) density distributions at the nozzle exit for the suction-wall and solid-wall nozzles.

Similarity of the flow velocity is one of the key requirements to ensure the similarity of GSI between wind tunnel experiments and actual flights in the VLEO. As a result, the uniformity of velocity is crucial to the reliability of the experimental results and must be considered in nozzle-flow optimization. In the present work, as defined in Equation (14), the region where the axial velocity reaches 99% of its maximum value (99% Vz_{max}) is defined as the uniform flow region (Ω). This region can be regarded as the effective test region for aerodynamic-force measurements of spacecraft in the VLEO.

$$\Omega = \{(z,r)|V_z(z,r) \geq 0.99V_{z,\max}\} \tag{14}$$

Figure 11a compares the axial velocity contours obtained for the suction-wall nozzle and the solid-wall nozzle. The introduction of wall suction increases the axial velocity

in the nozzle flow. A further examination of the boundaries of the uniform flow regions is presented in Figure 11b. The results indicate that wall suction leads to a substantial enlargement of the uniform flow region. Specifically, the maximum radius of the uniform flow region increases from 0.036 m to 0.040 m, corresponding to an increase of approximately 11%, while the total area of the uniform-flow region increases by about 60%. This enlargement is beneficial for wind tunnel experiments because a larger uniform-flow region enables the use of larger test models, thereby improving the accuracy of aerodynamic-force measurements. Figure 12 shows the mean free path contours for the two nozzles with different wall conditions. Compared with the solid-wall nozzle, wall suction produces a wider range of mean free path (approximately 0.02–0.12 m) within the uniform flow region, whose boundary is indicated by the dash dotted line. As a result, the corresponding Knudsen number can reach $Kn = 2$ for a reference length of 0.04 m, and up to $Kn = 12$ for 0.01 m. Such a range of Knudsen numbers indicates that the uniform flow region can reproduce flow conditions spanning from the transitional regime to the free-molecular regime, which are representative of the environment experienced by spacecraft in the VLEO.

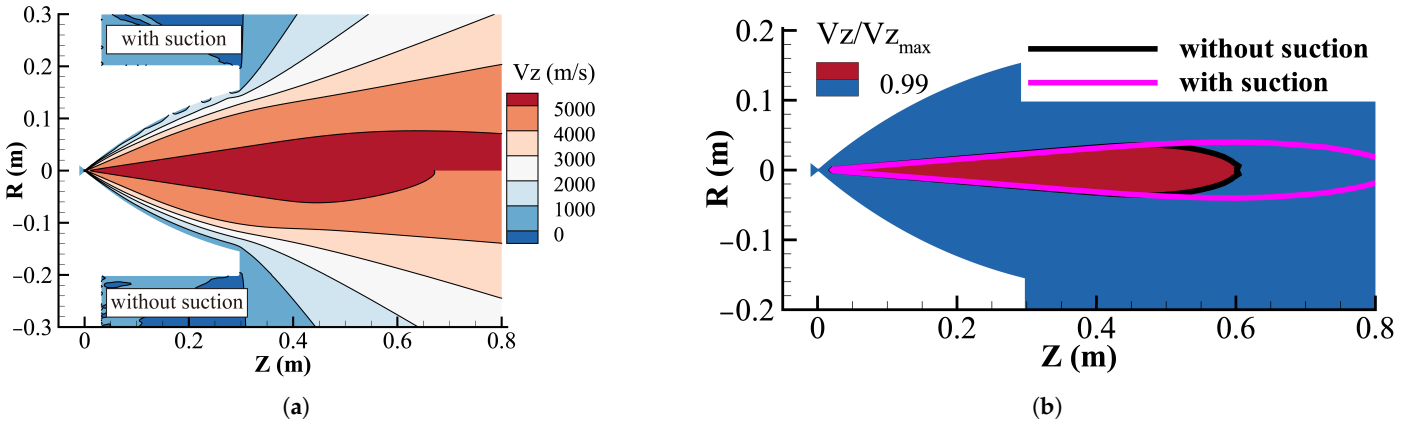

Figure 11. (**a**) Axial velocity contours and (**b**) boundaries of the uniform flow region for the solid-wall and suction-wall nozzles.

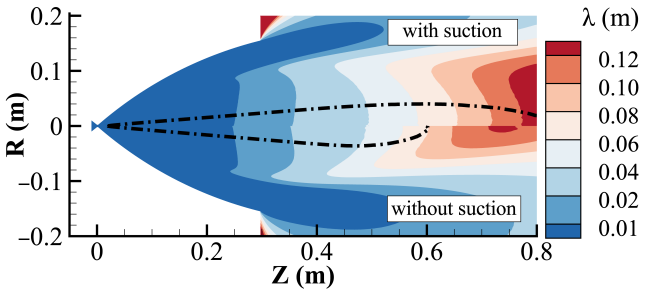

Figure 12. Mean free path contours for the solid-wall and suction-wall nozzles.

4.2. Nozzle Flow for P_0 = 50 kPa

To achieve freestream conditions with $Kn > 1$, wind tunnel experiments typically require small test models (on the order of 0.01 m). However, excessively small model sizes make it difficult to maintain geometric similarity. Consequently, it is necessary to further reduce the flow density in order to accommodate larger test models. According to quasi-one-dimensional flow theory, decreasing the inlet pressure is an effective approach for generating lower-density flows. Therefore, a simulation with $P_0 = 50$ kPa is conducted and the results are discussed below.

4.2.1. Flow Comparison Between $P_0 = 500$ kPa and $P_0 = 50$ kPa

We first compare the nozzle flows for total pressures of $P_0 = 50$ kPa and 500 kPa. Figure 13 shows the axial velocity contours and axial velocity distributions along the nozzle centerline for the two total pressures. A marked change in the flow is observed as the total pressure decreases. Figure 13 illustrates that the core-flow region diminishes into the interior of the nozzle, accompanied by a reduction in axial velocity. The centerline density distributions are shown in Figure 14a. The density inside the nozzle for P_0 = 50 kPa is significantly lower than that of P_0 = 500 kPa. As a result of low density and velocity, the flow inertia is too weak to offset the viscous forces [59], leading to a shrinkage of the core-flow region for $P_0 = 50$ kPa. It is also interesting to note that a noticeable variation in the density profiles is observed with decreasing pressure. As shown in Figure 14a, a slight increase in density is observed at Z = 0.7 m for P_0 = 500 kPa, which is caused by the shock wave (as discussed in Section 4.1.2). In contrast, the density profile only presents a plateau at Z = 0.3 m for P_0 = 50 kPa, suggesting the complete degeneration of shock wave. A similar phenomenon is also reported by Bykov [60]. Figure 14b presents the dimensionless density profiles at the nozzle exit, where the density is normalized by its value at $R = 0$ m. It can be seen that the density becomes nonuniform at the nozzle exit as the total pressure decreases to 50 kPa. Under this condition, the nozzle exit is almost entirely occupied by the boundary layer.

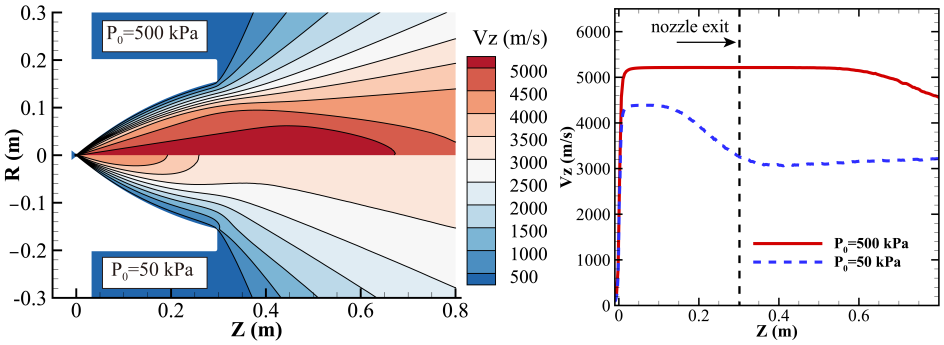

Figure 13. (**a**) Axial velocity contours and (**b**) axial velocity distributions along the nozzle centerline for $P_0 = 50$ kPa and $P_0 = 500$ kPa.

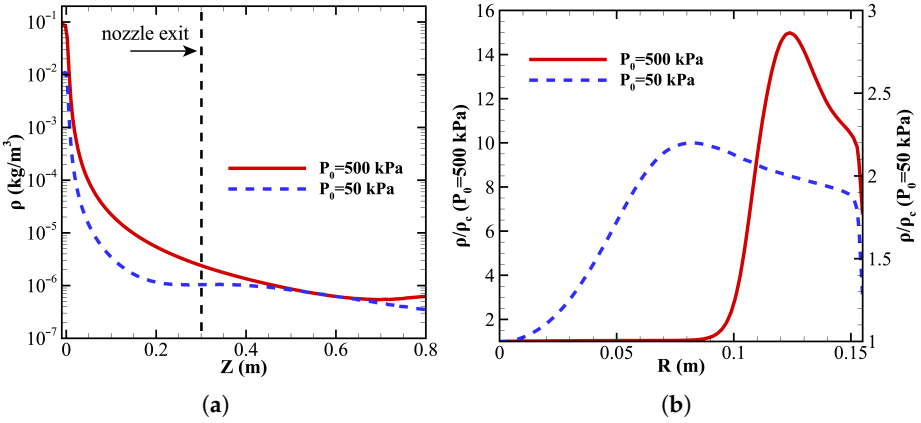

Figure 14. (**a**) Centerline density distributions and (**b**) nondimensional density distributions at the nozzle exit for different total pressures.

4.2.2. Effect of Wall Suction

The wall suction technique is also employed to improve the quality of nozzle flow. Figure 15 shows the axial velocity contours and the boundaries of the uniform flow regions for P_0 = 50 kPa under different wall conditions. Although the axial velocity in the nozzle divergent section increases for the suction-wall nozzle, the improvement in the uniform flow region is limited, as shown in Figure 15b. The boundaries of the uniform flow region are almost identical with and without wall suction. The limited effectiveness of wall suction can be attributed to the following reasons: (1) The suction velocity ratio (defined as the ratio of suction velocity to the flow velocity near the wall) is one of the key parameters governing the optimization effect [32]. Under highly rarefied conditions, the slip velocity increases due to rarefaction effects, resulting in a reduction in the suction velocity ratio and consequently weakening the effect of wall suction. (2) The lower gas density directly reduces the mass flow rate extracted through wall suction, further limiting its effectiveness. Therefore, alternative optimization strategies are required for ultra-low-density nozzle flows.

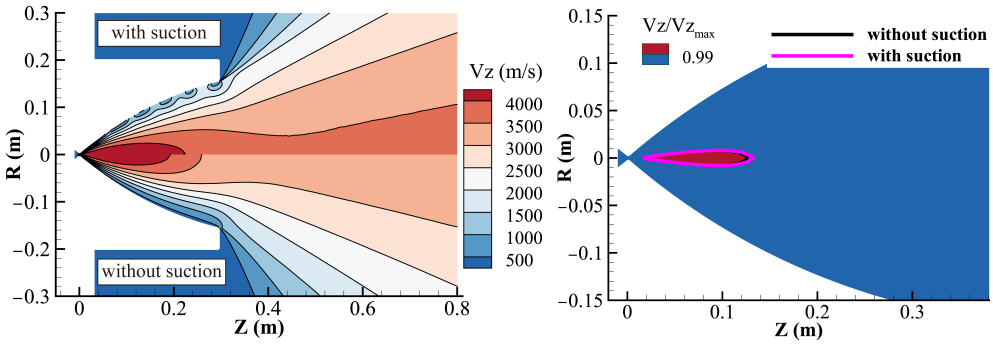

Figure 15. (**a**) Axial velocity contours and (**b**) boundaries of the uniform flow region for the solid-wall and suction-wall nozzles at P_0 = 50 kPa.

4.2.3. Effect of Wall Smoothing

The results presented in Section 4.2.2 indicate that wall suction has limited effectiveness in improving the flow quality at P_0 = 50 kPa. The analysis suggests that rarefaction effects, particularly velocity slip, are one of the primary causes of this limitation. It is well known that the momentum and thermal accommodation between the gas molecules and the wall have a great influence on the flow with significant rarefaction effects. On the one hand, from a macroscopic perspective, according to the first-order slip conditions (Equations (4) and (5)), a large slip velocity and jump temperature can be achieved by wall smoothing (that is, reducing the accommodation coefficient) for low-density flows where the mean free path is large. In contrast, for high-density flows with relatively small mean free paths, the influence of wall smoothing is much weaker. On the other hand, from a microscopic perspective, the probability p of the particles not accommodating with the wall after many collisions (i.e., specular reflection) can be expressed as

$$p = (1 - \alpha)^{\nu_s} \tag{15}$$

where α is the accommodation coefficient representing the probability of diffuse reflection, and ν_s is the collision frequency between the gas particles and the wall. When α is small but nonzero and the gas density is low ($\nu_s > 1$), p is greater than 0, and the gas particles still undergo specular reflection with a certain probability after many collisions. However, for high-density flows ($\nu_s \gg 1$), even though p is close to 0, i.e., the gas particles will accommodate with the wall because of abundant collisions. Therefore, wall smoothing is

considered a potentially effective strategy for improving the flow uniformity at $P_0 = 50$ kPa. In practice, wall smoothing can be achieved through surface-treatment techniques such as polishing and coating. In this work, based on the Maxwell model, nozzle flows with different accommodation coefficients ($\alpha = 1$, 0.4, 0.04, and 0) are investigated for two total pressures ($P_0 = 50$ kPa and 500 kPa).

Figure 16a shows the boundaries of the uniform flow region for various accommodation coefficients α at $P_0 = 50$ kPa. For $\alpha = 1$, the result of wall suction is also overlaid for comparison. The boundaries corresponding to $\alpha = 1$ with and without wall suction are almost indistinguishable in the figure. A careful examination of the area of uniform flow regions for the two cases shows a difference of only 5%, as given in Table 2. In contrast, the simulation results have clearly shown that the wall smoothing, by reducing the accommodation coefficient, is very effective in enlarging the uniform-flow region at $P_0 = 50$ kPa. For example, reducing α from 1 to 0.4 results in a 64% increase in the uniform-flow-region area. This value of α is physically grounded in experimental data showing that Al_2O_3 coatings achieve an accommodation coefficient of 0.4 during high-speed atomic oxygen interactions [61]. If the accommodation coefficient is further reduced by an order of magnitude to $\alpha = 0.04$, an over 3-fold larger uniform flow region can then be achieved. As shown in molecular dynamics studies [62,63], accommodation coefficients at this level are possible when the mass ratio between the incident gas and surface atoms is minimized, effectively inhibiting energy exchange. Under the idealized specular-reflection limit ($\alpha = 0$), the simulations predict a substantial enlargement of the uniform flow region. The case with $\alpha = 0$ is included mainly to illustrate the sensitivity of nozzle flow to GSI effects. Figure 16b compares the mean free path contours for the cases of $\alpha = 0$ and $\alpha = 1$. The boundary of the uniform flow region is also presented by the dash dotted line. The results show that a much larger mean free path, ranging from 0.1 to 0.8 m, is achieved within the uniform flow region for $\alpha = 0$. Based on the result for $\alpha = 0$, the uniform region is capable of generating a freestream of $Kn > 1$ for a reference length of 0.06 m.

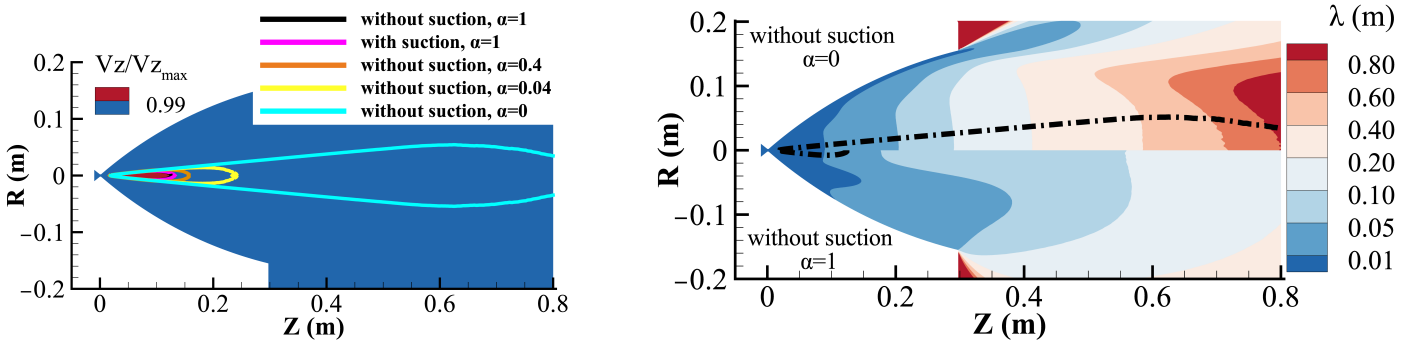

Figure 16. (**a**) Boundaries of uniform flow regions for different wall conditions and (**b**) mean free path contours for the specular wall ($\alpha = 0$) and diffuse wall ($\alpha = 1$) at $P_0 = 50$ kPa.

Table 2. Variation in the area of the uniform flow region for different wall conditions at $P_0 = 50$ kPa.

Wall Conditions	Area Increase (%)
Without suction (α = 1)	—
With suction (α = 1)	5%
Without suction (α = 0.4)	64%
Without suction (α = 0.04)	367%
Without suction (α = 0)	4754%

The results indicate that wall smoothing is more effective than wall suction in improving the uniformity of the nozzle flow with significant rarefaction effects. However, due to the low flow inertia at low densities, the uniform flow regions remain confined within the nozzle (see Figure 16a). This indicates that the nozzle geometry still requires further optimization for low-density flows. Previous studies on bell-shaped nozzles by Louisos et al. [64] have shown that reducing the length of the divergent section may enlarge the core flow region. Based on this finding, the effect of divergent section length on the uniform flow region will be investigated in future work.

The effects of wall smoothing on the flow for P_0 = 500 kPa are investigated as well. Figure 17 and Table 3 present the boundaries of the uniform flow region and the corresponding area variations, respectively. The results show that wall suction yields the maximum uniform-flow-region area. For the wall-smoothing cases, even when α is reduced to 0, the area of the uniform-flow region increases by only 27%, which is significantly smaller than the 60% increase achieved by wall suction. This indicates that, for nozzle flows with weak rarefaction effects, wall suction still outperforms wall smoothing in improving flow uniformity.

The findings of this study provide useful guidance for the design and optimization of RGWT nozzles intended for VLEO applications. First, the nozzle flow exhibits an underexpanded characteristic, where the extent of the core flow region determines the allowable dimensions of the test model. Second, the results indicate that wall smoothing is more effective than wall suction under highly rarefied flow conditions. This suggests that, for RGWT systems operating in extremely rarefied regimes, greater emphasis should be placed on wall surface treatment techniques to preserve flow uniformity and improve test-flow quality.

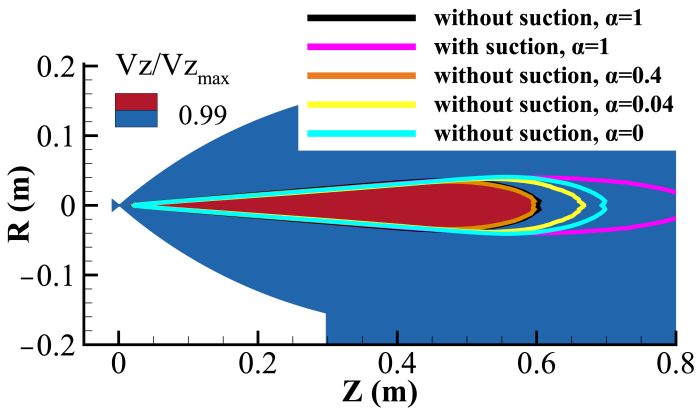

Figure 17. The uniform flow regions for different wall conditions at P_0 = 500 kPa.

Table 3. Variation in the area of the uniform flow region for different wall conditions at P_0 = 500 kPa.

Wall Conditions	Area Increase (%)
Without suction (α = 1)	—
With suction (α = 1)	60%
Without suction (α = 0.4)	−5%
Without suction (α = 0.04)	11%
Without suction (α = 0)	27%

5. Conclusions

The USPBGK-DSMC method is employed to investigate the ultra-high-speed flow in an RGWT for aerodynamic-force predictions of spacecraft in the VLEO. The results show that, due to a pressure drop of approximately seven orders of magnitude, the nozzle flow

exhibits multiscale characteristics, experiencing the flow regimes from the continuum to the transitional regime. Continuum breakdown parameter Kn_{GLL} varies by three orders of magnitude, confirming the multiscale nature of the nozzle flow. As a result, the continuum methods become invalid and multiscale particle methods are required to accurately solve the flow throughout the nozzle. The nozzle flow is found to be underexpanded and can be divided into a central uniform core and a surrounding region dominated by shock waves and boundary layers. At a total pressure of P_0 = 500 kPa, the surrounding region occupies nearly 50% of the nozzle exit area, degrading the flow quality. The traditional wall-suction technique proves effective in improving the flow uniformity by increasing the radius of the uniform flow region by 11% and its area by 60%. However, at a lower total pressure of P_0 = 50 kPa, enhanced rarefaction effects, particularly the increase in slip velocity, reduce the effectiveness of wall suction. In flows with strong rarefaction effects, gas–surface interactions become dominant. A wall-smoothing technique is proposed to improve the flow quality. The wall-smoothing technique, achieved by reducing the accommodation coefficient (α), substantially improves the flow uniformity. Reducing α from 1 to 0.4 increases the area of uniform flow region by 64%, which is much larger than the 5% achieved by wall suction. The results demonstrate that wall smoothing is more effective than wall suction in enhancing flow uniformity when rarefaction effects are significant.

It should be noted that the present study considers only atomic oxygen (O), as it is one of the dominant species in the VLEO environment. However, a more realistic simulation would require the inclusion of additional species, such as molecular nitrogen (N_2). Under the present stagnation conditions, the coexistence of O and (N_2) in the throat region is possible. The subsequent nozzle expansion may therefore be affected by inter-species interactions, including the potential Zeldovich exchange reaction, as well as differences in molecular mass and transport properties. As a result, the rarefied-flow characteristics and the nozzle optimization strategies could differ from those obtained in the present study. These will be investigated in future work.

Author Contributions: Conceptualization, W.S. and Y.H.; methodology, F.F. and Y.H.; software, Y.H.; validation, W.S. and C.Y.; formal analysis, W.S. and Y.H.; investigation, J.C. and X.M.; resources, Y.H. and H.H.; data curation, W.S.; writing—original draft preparation, W.S.; writing—review and editing, W.S., Y.H., Q.S., and H.H.; visualization, W.S.; supervision, Y.H. and H.H.; project administration, Y.H.; funding acquisition, C.Y. and Y.H. All authors have read and agreed to the published version of the manuscript.

Funding: This research was funded by the Pioneering Science and Technology Strategic Priority Program of the Chinese Academy of Sciences (Grant No. XDA0470102) and the Young Scientists Fund of the National Natural Science Foundation of China (Grant No. 12202458).

Data Availability Statement: Data available from the corresponding author upon reasonable request.

Conflicts of Interest: The authors declare no conflicts of interest. The funders had no role in the design of the study; in the collection, analyses, or interpretation of data; in the writing of the manuscript; or in the decision to publish the results.

References

1. Llop, J.V.; Roberts, P.C.; Hao, Z.; Tomas, L.R.; Beauplet, V. Very low earth orbit mission concepts for earth observation: Benefits and challenges. In Proceedings of the Reinventing Space Conference, London, UK, 18–21 November 2014; pp. 18–21.
2. Muñoz, V.C.; González, D.; Becedas, J.; Dominguez, R.M.; Roberts, P.C.E.; Crisp, N.H.; Oiko, V.T.A.; Edmondson, S.; Worrall, S.D.; Haigh, S.; et al. Attitude control for satellites flying in VLEO using aerodynamic surfaces. *J. Br. Interplanet. Soc.* **2020**, *73*, 103–112.
3. Berthoud, L.; Hills, R.; Bacon, A.; Havouzaris-Waller, M.; Hayward, K.; Gayrard, J.D.; Arnal, F.; Combelles, L. Are Very Low Earth Orbit (VLEO) satellites a solution for tomorrow's telecommunication needs? *CEAS Space J.* **2022**, *14*, 609–623. [CrossRef]

4. Rapisarda, C.; Roberts, P.C.; Smith, K.L. Design and optimisation of a passive Atmosphere-Breathing Electric Propulsion (ABEP) intake. *Acta Astronaut.* **2023**, *202*, 77–93. [CrossRef]
5. Filatyev, A.; Golikov, A.; Erofeev, A.; Khartov, S.; Lovtsov, A.; Padalitsa, D.; Skvortsov, V.; Yanova, O. Research and development of aerospace vehicles with air breathing electric propulsion: Yesterday, today, and tomorrow. *Prog. Aerosp. Sci.* **2023**, *136*, 100877. [CrossRef]
6. Walsh, J.; Berthoud, L.; Allen, C. Drag reduction through shape optimisation for satellites in Very Low Earth Orbit. *Acta Astronaut.* **2021**, *179*, 105–121. [CrossRef]
7. Jiang, Y.; Zhang, J.; Tian, P.; Liang, T.; Li, Z.; Wen, D. Aerodynamic drag analysis and reduction strategy for satellites in Very Low Earth Orbit. *Aerosp. Sci. Technol.* **2023**, *132*, 108077. [CrossRef]
8. Li, X.; Geng, J.; Yue, Y.; Han, N.; Sun, W.; Yang, C.; Hu, Y.; Feng, G.; Meng, X.; Cao, J.; et al. Structural and configurational optimization of spacecrafts in Very Low Earth Orbit using Atmosphere-Breathing Electric Propulsion. *Acta Astronaut.* **2025**, *233*, 82–98. [CrossRef]
9. Steiger, C.; Romanazzo, M.; Floberghagen, R.; Fehringer, M.; Emanuelli, P. The deorbiting of GOCE-a spacecraft operations perspective. *ESA Spec. Publ.* **2015**, *728*, 19.
10. Yamamoto, T.; Konoue, K.; Imamura, S.; Hayato, A.; Ohtani, T. Conceptual study of JAXA's VLEO platform: Flight results of super low-altitude test satellite (SLATS) and advancement towards practical applications. In *Proceedings of the Small Satellites Systems and Services Symposium (4S 2024)*; SPIE: Bremen, Germany, 2025; Volume 13546, pp. 515–527.
11. Binder, T.; Boldini, P.C.; Romano, F.; Herdrich, G.; Fasoulas, S. Transmission probabilities of rarefied flows in the application of atmosphere-breathing electric propulsion. *AIP Conf. Proc.* **2016**, *1786*, 190011. [CrossRef]
12. Bird, G.A. *Molecular Gas Dynamics and the Direct Simulation of Gas Flows*; Oxford University Press: New York, NY, USA, 1994. [CrossRef]
13. Ozawa, T.; Suzuki, T.; Fujita, K. Aerodynamic measurements and computational analyses in hypersonic rarefied flows. *AIAA J.* **2015**, *53*, 3327–3337. [CrossRef]
14. Coumar, S. Study of Physical Mechanisms Induced by a Plasma Actuator for Super/Hypersonic Rarefied Flows Applied to Atmospheric Entries. Ph.D. Thesis, Université d'Orléans, Orléans, France, 2017.
15. Han, N.; Cao, J.; Meng, X.; Liu, H.; Zhang, S.; Huang, H. Density estimation of an ultrahigh-speed rarefied flow field based on force analysis of a pendulum sphere. *Vacuum* **2023**, *211*, 111919. [CrossRef]
16. Zhang, S.; Yu, X.; Yan, H.; Huang, H.; Liu, H. Molecular tagging velocimetry of NH fluorescence in a high-enthalpy rarefied gas flow. *Appl. Phys. B* **2017**, *123*, 122. [CrossRef]
17. Boyd, I.D.; Chen, G.; Candler, G.V. Predicting failure of the continuum fluid equations in transitional hypersonic flows. *Phys. Fluids* **1995**, *7*, 210–219. [CrossRef]
18. Schwartzentruber, T.E.; Boyd, I.D. A hybrid particle-continuum method applied to shock waves. *J. Comput. Phys.* **2006**, *215*, 402–416. [CrossRef]
19. Titov, E.; Zeifman, M.; Levin, D. Application of the kinetic and continuum techniques to the multi-scale flows in MEMS devices. In Proceedings of the 43rd AIAA Aerospace Sciences Meeting and Exhibit, Reno, NV, USA, 10–13 January 2005; p. 1399. [CrossRef]
20. Wijesinghe, H.S.; Hadjiconstantinou, N.G. Discussion of hybrid atomistic-continuum methods for multiscale hydrodynamics. *Int. J. Multiscale Comput. Eng.* **2004**, *2*, 189–202. [CrossRef]
21. Kumar, R.; Titov, E.; Levin, D. Development of a particle–particle hybrid scheme to simulate multiscale transitional flows. *AIAA J.* **2013**, *51*, 200–217. [CrossRef]
22. Xu, K.; Huang, J.C. A unified gas-kinetic scheme for continuum and rarefied flows. *J. Comput. Phys.* **2010**, *229*, 7747–7764. [CrossRef]
23. Guo, Z.; Xu, K.; Wang, R. Discrete unified gas kinetic scheme for all Knudsen number flows: Low-speed isothermal case. *Phys. Rev. E* **2013**, *88*, 033305. [CrossRef] [PubMed]
24. Mieussens, L. Discrete-Velocity Models and Numerical Schemes for the Boltzmann-BGK Equation in Plane and Axisymmetric Geometries. *J. Comput. Phys.* **2000**, *162*, 429–466. [CrossRef]
25. Titarev, V. Conservative numerical methods for model kinetic equations. *Comput. Fluids* **2007**, *36*, 1446–1459. [CrossRef]
26. Shakhov, E.M. Generalization of the Krook kinetic relaxation equation. *Fluid Dyn.* **1968**, *3*, 95–96. [CrossRef]
27. Holway, L.H., Jr. New Statistical Models for Kinetic Theory: Methods of Construction. *Phys. Fluids* **1966**, *9*, 1658–1673. [CrossRef]
28. Macrossan, M. *v*-DSMC: A Fast Simulation Method for Rarefied Flow. *J. Comput. Phys.* **2001**, *173*, 600–619. [CrossRef]
29. Gallis, M.A.; Torczynski, J.R. Investigation of the ellipsoidal-statistical Bhatnagar–Gross–Krook kinetic model applied to gas-phase transport of heat and tangential momentum between parallel walls. *Phys. Fluids* **2011**, *23*, 30601. [CrossRef]
30. Jenny, P.; Torrilhon, M.; Heinz, S. A solution algorithm for the fluid dynamic equations based on a stochastic model for molecular motion. *J. Comput. Phys.* **2010**, *229*, 1077–1098. [CrossRef]
31. Fei, F.; Zhang, J.; Li, J.; Liu, Z. A unified stochastic particle Bhatnagar-Gross-Krook method for multiscale gas flows. *J. Comput. Phys.* **2020**, *400*, 108972. [CrossRef]

32. Bottorff, M.R.; Rogers, K.W. *Theoretical and Experimental Investigation of Boundary Layer Control in Low-Density Nozzles by Wall Suction and Cooling*; Technical Report; National Aeronautics and Space Administration: Hanceville, AL, USA, 1964.
33. Stalder, J.R.; Goodwin, G.; Creager, M.O. *Heat Transfer to Bodies in a High-Speed Rarified-Gas Stream*; Technical Report; National Aeronautics and Space Administration: Huntsville, AL, USA, 1952.
34. Bottorff, M.R.; Lindsay, A.I.; Rogers, K.W. *Study of Porous Wall Low Density Wind Tunnel Diffusers*; Technical Report; National Aeronautics and Space Administration: Huntsville, AL, USA, 1966.
35. Stalder, J.R. The Use of Low-Density Wind Tunnels in Aerodynamic Research. In *Rarefied Gas Dynamics, Proceedings of the First International Symposium Held at Nice*; Pergammon Press: New York, NY, USA, 1960; pp. 1–20.
36. Alexander, F.J.; Garcia, A.L.; Alder, B.J. Cell size dependence of transport coefficients in stochastic particle algorithms. *Phys. Fluids* **1998**, *10*, 1540–1542. [CrossRef]
37. Garcia, A.L.; Wagner, W. Time step truncation error in direct simulation Monte Carlo. *Phys. Fluids* **2000**, *12*, 2621–2633. [CrossRef]
38. Fei, F.; Jenny, P. A hybrid particle approach based on the unified stochastic particle Bhatnagar-Gross-Krook and DSMC methods. *J. Comput. Phys.* **2021**, *424*, 109858. [CrossRef]
39. Fei, F.; Hu, Y.; Jenny, P. A unified stochastic particle method based on the Bhatnagar-Gross-Krook model for polyatomic gases and its combination with DSMC. *J. Comput. Phys.* **2022**, *471*, 111640. [CrossRef]
40. Fei, F.; Liu, D.; Xie, L.; Ren, Z.; Hu, Y. A unified stochastic particle method for polyatomic gas mixtures. *Comput. Phys. Commun.* **2026**, *321*, 110029. [CrossRef]
41. Boyd, I.D. Conservative species weighting scheme for the direct simulation Monte Carlo method. *J. Thermophys. Heat Transf.* **1996**, *10*, 579–585. [CrossRef]
42. Jin, X.; Cheng, X.; Huang, Y.; Wang, Q.; Wang, B.; Shen, Q. Numerical analysis of inlet flows at different altitudes in the upper atmosphere. *Phys. Fluids* **2023**, *35*, 093605. [CrossRef]
43. Rothe, D.E. Electron-beam studies of viscous flow in supersonic nozzles. *AIAA J.* **1971**, *9*, 804–811. [CrossRef]
44. Sun, W.; Liu, X.; Long, J.; Wang, X.; Sun, Q.; Huang, H.; Li, Y.; Hu, Y. Kinetic Simulation of Nozzle Flow in a Micronewton-Class Cold Gas Thruster. *AIAA J.* **2024**, *62*, 4533–4542. [CrossRef]
45. Lofthouse, A.J.; Boyd, I.D.; Wright, M.J. Effects of continuum breakdown on hypersonic aerothermodynamics. *Phys. Fluids* **2007**, *19*, 027105. [CrossRef]
46. Anderson, J. *EBOOK: Fundamentals of Aerodynamics (SI Units)*; McGraw Hill: New York, NY, USA, 2011.
47. Chong, X. Subsonic choked flow in the microchannel. *Phys. Fluids* **2006**, *18*, 127104. [CrossRef]
48. Zhao, W.; Hong, Q.; Yang, C.; Sun, Q.; Hu, Y. Collision integrals of electronically excited atoms in air plasmas. I. N–N and O–O interactions. *Plasma Sources Sci. Technol.* **2023**, *32*, 125002. [CrossRef]
49. Tsuboi, N.; Matsumoto, Y. Experimental and Numerical Study of Hypersonic Rarefied Gas Flow over Flat Plates. *AIAA J.* **2005**, *43*, 1243–1255. [CrossRef]
50. Bird, G.A. Breakdown of translational and rotational equilibrium in gaseous expansions. *AIAA J.* **1970**, *8*, 1998–2003. [CrossRef]
51. Garcia, A.L.; Alder, B.J. Generation of the Chapman–Enskog distribution. *J. Comput. Phys.* **1998**, *140*, 66–70. [CrossRef]
52. Boyd, I.D. Predicting Breakdown of the Continuum Equations Under Rarefied Flow Conditions. *AIP Conf. Proc.* **2003**, *663*, 899–906. [CrossRef]
53. Tiwari, S. Coupling of the Boltzmann and Euler equations with automatic domain decomposition. *J. Comput. Phys.* **1998**, *144*, 710–726. [CrossRef]
54. Dogra, V.K.; Moss, J.N. Hypersonic rarefied flow about plates at incidence. *AIAA J.* **1991**, *29*, 1250–1258. [CrossRef]
55. Donaldson, C.d.; Snedeker, R.S. A study of free jet impingement. Part 1. Mean properties of free and impinging jets. *J. Fluid Mech.* **1971**, *45*, 281–319. [CrossRef]
56. Ashkenas, H.; Sherman, F.S. *Structure and Utilization of Supersonic Free Jets in Low Density Wind Tunnels*; Technical Report; National Aeronautics and Space Administration: Huntsville, AL, USA, 1965.
57. Wilkes Inman, J.; Danehy, P.; Nowak, R.; Alderfer, D. Fluorescence imaging study of impinging underexpanded jets. In Proceedings of the 46th AIAA Aerospace Sciences Meeting and Exhibit, Reno, NV, USA, 7–10 January 2008; p. 619.
58. Franquet, E.; Perrier, V.; Gibout, S.; Bruel, P. Free underexpanded jets in a quiescent medium: A review. *Prog. Aerosp. Sci.* **2015**, *77*, 25–53. [CrossRef]
59. Louisos, W.F.; Hitt, D.L. Viscous effects on performance of two-dimensional supersonic linear micronozzles. *J. Spacecr. Rocket.* **2008**, *45*, 706–715. [CrossRef]
60. Bykov, N.Y.; Gorbachev, Y.E.; Fyodorov, S.A. Highly underexpanded rarefied jet flows. *Front. Mech. Eng.* **2023**, *9*. [CrossRef]
61. Minton, T.K.; Schwartzentruber, T.E.; Xu, C. On the utility of coated POSS-polyimides for vehicles in very low earth orbit. *ACS Appl. Mater. Interfaces* **2021**, *13*, 51673–51684. [CrossRef] [PubMed]
62. Liao, M.; Grenier, R.; To, Q.D.; de Lara-Castells, M.P.; Léonard, C. Helium and Argon Interactions with Gold Surfaces: Ab Initio-Assisted Determination of the He–Au Pairwise Potential and Its Application to Accommodation Coefficient Determination. *J. Phys. Chem. C* **2018**, *122*, 14606–14614. [CrossRef]

63. Chen, Y.; Gibelli, L.; Borg, M.K. Impact of random nanoscale roughness on gas-scattering dynamics. *Phys. Rev. E* **2024**, *109*, 065308. [CrossRef] [PubMed]
64. Louisos, W.F.; Hitt, D.L. Numerical studies of supersonic flow in bell-shaped micronozzles. *J. Spacecr. Rocket.* **2014**, *51*, 491–500. [CrossRef]